Labyrinthine domains in ferroelectric nanoparticles: Manifestation of a gradient-induced morphological transition

Eugene A. Eliseev,[1] Yevhen M. Fomichov,[1] Sergei V. Kalinin,[2] Yulian M. Vysochanskii,[3] Peter Maksymovich,[2] and Anna N. Morozovska[4,5,*]

[1]*Institute for Problems of Materials Science, National Academy of Sciences of Ukraine, Krjijanovskogo 3, 03142 Kyiv, Ukraine*

[2]*The Center for Nanophase Materials Sciences, Oak Ridge National Laboratory, Oak Ridge, Tennessee 37831, USA*

[3]*Institute of Solid State Physics and Chemistry, Uzhgorod University, 88000 Uzhgorod, Ukraine*

[4]*Institute of Physics, National Academy of Sciences of Ukraine, 46, pr. Nauky, 03028 Kyiv, Ukraine*

[5]*Bogolyubov Institute for Theoretical Physics, National Academy of Sciences of Ukraine, 14-b Metrolohichna str. 03680 Kyiv, Ukraine*

(Received 11 January 2018; revised manuscript received 8 June 2018; published 2 August 2018)

In the framework of the Landau-Ginzburg-Devonshire (LGD) approach we studied finite-size effects of the phase diagram and domain structure evolution in spherical nanoparticles of a uniaxial ferroelectric. The particle surface is covered by a layer of screening charge characterized by finite screening length. The phase diagram, calculated in coordinates particle radius and screening length has a wide region of versatile polydomain structures separating single-domain ferroelectric and nonpolar paraelectric phases. Unexpectedly, we revealed a region of irregular labyrinthine domains in the nanoparticles of uniaxial ferroelectric $CuInP_2S_6$ with the first-order paraelectric-ferroelectric phase transition. We established that the origin of labyrinthine domains is the mutual balance of LGD, polarization gradient, and electrostatic energies. The branching of the domain walls appears and increases rapidly when the polarization gradient energy decreases below the critical value. Allowing for the generality of the LGD approach, we expect that the gradient-induced morphological transition can be the source of labyrinthine domain appearance in many spatially confined ferroics with long-range order parameter, including relaxors, ferromagnetics, antiferrodistortive materials, and materials with incommensurate ferroic phases.

DOI: 10.1103/PhysRevB.98.054101

I. INTRODUCTION

The ferroic materials described by Landau theory of symmetry breaking have a substantial impact on fundamental science and various applications. Different types of topological defects in different ferroics (ferromagnets, ferroelectrics, ferroelastics) are even more numerous and enigmatic than different types of symmetry breaking, and consequently they become one of the key fundamental problems and hot topics in the scientific community [1,2].

Complementary to the topological point defects [1], domain walls can be considered as extended two-dimensional topological defects in ferroics (see, e.g., Chap. 8 in Ref. [2] and references therein). Vortices and vertices composed by the closure of four domain walls have been observed experimentally and described theoretically in a bulk and nanosized ferroelectrics [3–7]. Stable surface-induced labyrinthine domain structures were observed by piezoresponse force microscopy (PFM) in ergodic ferroelectrics relaxors and explained by the presence of a higher-order term in free-energy expansion that gives rise to the polarization modulations [8]. Fractal domain structures are sometimes observed in multiferroic thin films [9] and near the surface of relaxors close to the relaxor-ferroelectric boundary [10], but the labyrinthine domains with a single characteristic length scale were observed by PFM in ergodic relaxors only [8]. These labyrinthine structures can coexist with classical ferroelectric domains closer to the ferroelectric composition limit [11,12]. The labyrinthine domain structure was predicted theoretically in thin films of incommensurate ferroelectrics [13] and bilayered ferroelectrics [14], being similar to those observed in ultrathin magnetic films [15].

However, we did not find any experimental observation or theoretical prediction of labyrinthine domains in the nanoparticles of ordered ferroelectrics, the intriguing polar and dielectric properties of which attract permanent attention of researchers. Classical examples are the unexpected experimental results of Yadlovker and Berger [16–18], which reveal the enhancement of polar properties of cylindrical nanoparticles of Rochelle salt. Frey and Payne [19], Zhao *et al.* [20], Drobnich *et al.* [21], Erdem *et al.* [22], and Golovina *et al.* [23–25] demonstrate the possibility to control the phase transitions (including new polar phases appearance) for $BaTiO_3$, $S_2P_2S_6$, $PbTiO_3$, and $KTa_{1-x}Nb_xO_3$ nanopowders and nanoceramics by finite-size effects.

The theory of finite-size effects in nanoparticles allows one to establish the physical origin of the polar and dielectric properties anomalies, and phase diagrams changes appeared under the nanoparticles sizes decrease. Using the continual phenomenological approach Perriat *et al.* [26], Huang *et al.* [27,28], Wenhui Ma [29], Eliseev *et al.* [30] and Morozovska *et al.* [31–33] have shown that the changes of the transition temperatures and the enhancement or weakening of polar properties in single-domain spherical and cylindrical nanoparticles are conditioned by various physical mechanisms, such as correlation effect, depolarization field, flexoelectricity,

*Corresponding author: anna.n.morozovska@gmail.com

electrostriction, surface tension, and Vegard-type chemical pressure.

Notably the depolarization field always decreases ferroelectric polarization and transition temperature, especially under the presence of imperfect screening [34–36]. For the majority of models the particles were covered with perfect electrodes so that their single-domain state would be stable. Only a few models describing the imperfect screening effect in nanoparticles have evolved [34–36].

To fill the gap in the knowledge, below we analyze the phase diagram and domain structure evolution in spherical nanoparticles of uniaxial ferroelectric $CuInP_2S_6$ (CIPS). We assumed that the particle surface is covered by a layer of screening charge characterized by finite screening length. The imperfect screening and finite-size effects are studied using the Landau-Ginzburg-Devonshire (LGD) approach combined with the electrostatic equations. We revealed that a regular stripe domain structure transforms avalanchelike into a labyrinth pattern with a gradient term decrease below the critical value and classified the event as a gradient-induced morphological transition.

The applicability of the LGD approach for thin films and nanoparticles with radius less than 2–10 nm is corroborated by the fact that the critical sizes of the long-range order appearance and properties calculated from atomistic [37–41] and phenomenological [30–33,42,43] theories are in a good agreement with each other as well as with experimental results for nanosized ferromagnetics [44] and ferroelectrics [16–20,22,45]. Both atomistic simulations and LGD description are absent for CIPS nanoparticles.

II. THEORETICAL APPROACH

Let us consider a CIPS nanoparticle of radius R with a one-component ferroelectric polarization $P_3(\mathbf{r})$ directed along the crystallographic axis 3 [Fig. 1(a)]. The particles are covered by a layer of screening charge with a surface charge density σ characterized by a nonzero screening length λ. The specific nature of the surface charge can be, e.g., Bardeen-type surface states [46]. The screening charges can be localized at surface states caused by the strong band bending via depolarization field [47–51], at which λ can be much smaller ($\leqslant$0.1 nm) than a lattice constant ($\sim$0.5 nm) [34]. Concrete expression for λ can be derived in, e.g., the Stephenson-Highland ionic adsorption model [52–54], by the linearization of σ, as

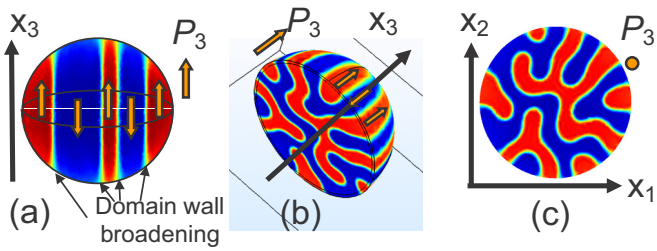

FIG. 1. Labyrinthine domains in a spherical CIPS nanoparticle. (a) Polar cross-section, (b) semispherical view, and (c) equatorial cross-section. Radius $R = 10$ nm, screening length $\lambda = 0.03$ nm, room temperature 293 K. CIPS parameters are listed in Table I.

$\sigma \approx -\varepsilon_0\varphi/\lambda$, where $\lambda^{-1} \approx \sum_i \frac{(eZ_i)^2}{4\varepsilon_0 A_i k_B T}[1 - \tanh^2(\frac{\Delta G_i^{00}}{2k_B T})]$, Z_i is the ionization number of the surface ions, $1/A_i$ is their saturation densities, ΔG_i^{00} is the free energy of the surface ion formation, and ε_0 is a universal dielectric constant. In the general case λ depends on temperature T and screening charges nature. Since we do not know the temperature dependence of λ, we performed calculations for λ changing in the range $10^{-3} - 1$ nm.

For a layered perovskite with layers plane (001) and ferroelectric dipoles directed in the out-of-plane direction, we can assume that the dependence of the in-plane components of electric polarization on the electric field E_i is linear, $P_i = \varepsilon_0(\varepsilon_b - 1)E_i$ $(i = 1, 2)$, where an isotropic background permittivity ε_b is relatively small, $\varepsilon_b \leqslant 10$ [55]. Polarization component $P_3(\mathbf{r})$ contains background and soft mode contributions. The electric displacement vector has the form $\mathbf{D} = \varepsilon_0\varepsilon_b\mathbf{E} + \mathbf{P}$ inside the particle and $\mathbf{D} = \varepsilon_0\varepsilon_e\mathbf{E}$ outside it; ε_e is the relative dielectric permittivity of external media equal to unity for air or vacuum.

The Euler-Lagrange equation for the ferroelectric polarization $P_3(\mathbf{r})$ follows from the minimization of LGD free energy functional $G = G_{\text{Landau}} + G_{\text{grad}} + G_{\text{el}} + G_{\text{es+flexo}}$, that includes Landau energy G_{Landau}, polarization gradient energy contribution G_{grad}, electrostatic contribution G_{el}, and elastic, electrostriction, and flexoelectric contributions $G_{\text{es+flexo}}$ (see, e.g., [30,35,56]):

$$G_{\text{Landau}} = \int_{|\vec{r}|<R} d^3r\left(\frac{\alpha}{2}P_3^2 + \frac{\beta}{4}P_3^4 + \frac{\gamma}{6}P_3^6\right), \tag{1a}$$

$$G_{\text{grad}} = \int_{|\vec{r}|<R} d^3r\left\{\frac{g_{11}}{2}\left(\frac{\partial P_3}{\partial x_3}\right)^2 + \frac{g_{44}}{2}\left[\left(\frac{\partial P_3}{\partial x_2}\right)^2 + \left(\frac{\partial P_3}{\partial x_1}\right)^2\right]\right\}, \tag{1b}$$

$$G_{\text{el}} = -\int_{|\vec{r}|<R} d^3r\left(P_3E_3 + \frac{\varepsilon_0\varepsilon_b}{2}E_iE_i\right) - \int_{|\vec{r}|=R} d^2r\left(\frac{\varepsilon_0\varphi^2}{2\lambda}\right) - \frac{\varepsilon_0\varepsilon_e}{2}\int_{|\vec{r}|>R} E_iE_i d^3r, \tag{1c}$$

$$G_{\text{es+flexo}} = \int_{|\vec{r}|<R} d^3r\left[-\frac{s_{ijkl}}{2}\sigma_{ij}\sigma_{kl} - Q_{ij3}\sigma_{ij}P_3^2 - F_{ijk3}\left(\sigma_{ij}\frac{\partial P_3}{\partial x_k} - P_3\frac{\partial \sigma_{ij}}{\partial x_k}\right)\right]. \tag{1d}$$

Here E_i are electric field components related to electric potential φ as $E_i = -\partial\varphi/\partial x_i$. The coefficient α linearly depends on temperature T, $\alpha = \alpha_T(T - T_C)$, where T_C is the Curie temperature. The coefficient β is temperature independent and negative, since CIPS undergoes the first-order transition to the paraelectric phase. Coefficient γ and gradient coefficients g_{11} and g_{44} are positive and temperature independent. An isotropic approximation, $g_{44} \approx g_{55}$, in the (001) plane was taken for monoclinic CIPS structure. σ_{ij} is the stress tensor in Eq. (1d). We omit the evident form of $G_{\text{es+flexo}}$ for the sake of simplicity, it is listed in Refs. [57–59]. Since the values of the electrostriction and flexoelectric tensor components, Q_{ijkl}

TABLE I. LGD parameters for bulk ferroelectric $CuInP_2S_6$, used in calculations.

ε_b	α_T (C^{-2} m J/K)	T_C (K)	β (C^{-4} m^5 J)	γ (C^{-6} m^9 J)	g_{11}(m^3/F) [62]	g_{44} (m^3/F)
7	1.569×10^7	302	-1.8×10^{12}	2.2×10^{15}	1.0×10^{-10}	Vary in the range 0.3–3 $\times 10^{-11}$

and F_{ijkl}, are unknown for CIPS, we performed numerical calculations using the finite element method with the coefficients varied in a physically reasonable range ($|F_{ijkl}| \leqslant 10^{11}$ m^3/C and $|Q_{ijkl}| \leqslant 0.1$ m^4/C^2). Results proved the insignificant impact of electrostriction and flexoelectric coupling on domain morphology [60]. Other LGD parameters for a bulk ferroelectric CIPS were taken from Ref. [61] and are listed in Table I.

Allowing for the Khalatnikov mechanism of polarization relaxation, the corresponding Euler-Lagrange equation for $P(\mathbf{r}_3)$ becomes a time-dependent LGD equation [63]:

$$\Gamma\frac{\partial P_3}{\partial t} + \alpha(T)P_3 + \beta P_3^3 + \gamma P_3^5 - g_{44}\left(\frac{\partial^2}{\partial x_1^2} + \frac{\partial^2}{\partial x_2^2}\right)P_3 - g_{11}\frac{\partial^2 P_3}{\partial x_3^2} = E_3. \quad (2)$$

The Khalatnikov coefficient Γ determines the relaxation time of polarization $\tau_K = \Gamma/|\alpha|$, that typically varies in the range 10^{-11}–10^{-13} s far from T_C. The boundary condition for P at the spherical surface is natural, $\partial\vec{P}/\partial\mathbf{n}|_{r=R} = 0$, where $\mathbf{n}$ is the outer normal to the surface.

Electric potential φ satisfies a Poisson equation inside the particle,

$$\varepsilon_0\varepsilon_b\Delta\varphi = -\frac{\partial P}{\partial x_3}, \quad (3a)$$

and Laplace equation outside it,

$$\Delta\varphi = 0. \quad (3b)$$

The three-dimensional Laplace operator is denoted by the symbol Δ. Equations (3) are supplemented by the condition of potential continuity at the particle surface, $(\varphi_{ext} - \varphi_{int})|_{r=R} = 0$. The boundary condition for the normal components of electric displacements is $[\mathbf{n}(\mathbf{D}_{ext} - \mathbf{D}_{int}) + \sigma]_{r=R} = 0$, where the surface charge density $\sigma = -\varepsilon_0\varphi/\lambda$.

In fact the screening length λ decrease improves the screening conditions, which leads to a decrease in the depolarization field and hence the domains eventually disappear, giving way to a more energetically favorable single-domain state (see, e.g., Fig. 2 in Ref. [58]).

III. NUMERICAL RESULTS AND DISCUSSION

A. Main features of phase diagrams at different temperatures

Phase diagrams were studied at different temperatures in the range 300–200 K. Unfortunately we do not know the temperature dependence of λ, and so we perform all calculations regarding λ changing in the range 10^{-3}–1 nm. The phase diagram of CIPS nanoparticles calculated at $T = 293$ and 200 K in coordinates radius R and screening length λ is shown in Figs. 2(a) and 2(b), respectively.

At room temperature the phase diagram has an unexpectedly wide region of stable polydomain states (PDFE) separating single-domain ferroelectric (SDFE) and nonpolar paraelectric (PE) phases [see Fig. 2(a)]. The bottom row shows the typical changes of polarization distribution in the equatorial cross-section of the nanoparticle with $R = 5$ nm, which happens with increase of λ. A single-domain state is stable at very small $\lambda < 0.01$ nm, a two-domain structure (electric quadrupole) is stable in the interval $0.01 < \lambda < 0.017$ nm, a three-domain structure (electric octupole) exists at $0.017 < \lambda < 0.019$ nm, and $2N$-multipolar domain stripes are stable at

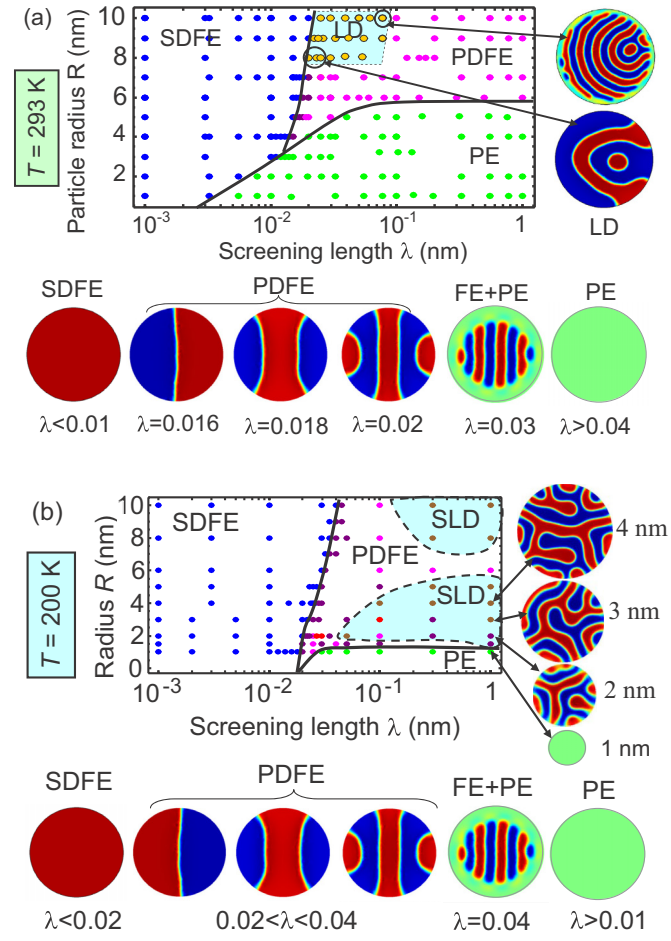

FIG. 2. Phase diagram of CIPS nanoparticles in coordinates radius R and screening length λ calculated for the gradient coefficient $g_{44} = 2 \times 10^{-11}$ m^3/F and temperatures 293 K (a) and 200 K (b). The ferroelectric single-domain (SDFE), ferroelectric poly-domain (PDFE), and paraelectric (PE) phases are shown by different colors of the circles. The labyrinthine domains (LD) are located within dashed light-blue regions. The bottom rows shows typical polarization distributions in the equatorial cross-sections of the nanoparticles with radius $R = 5$ nm and different values of λ (in nanometers). CIPS parameters are listed in Table I.

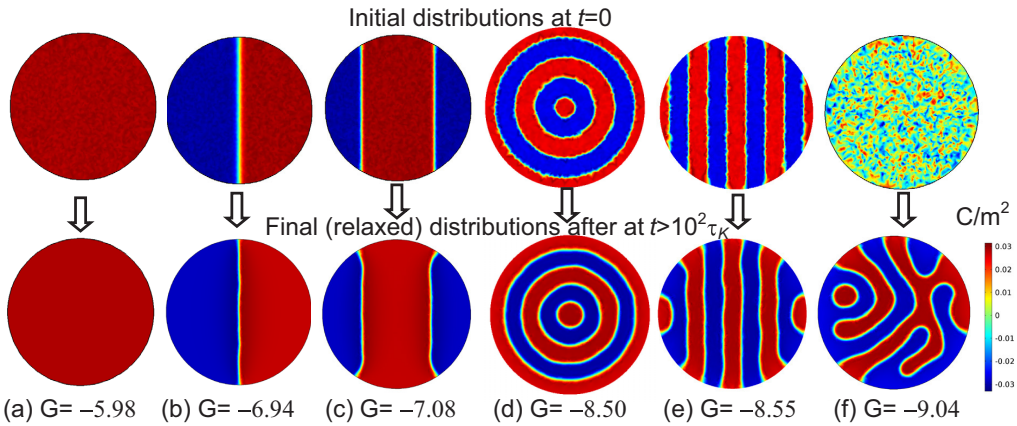

FIG. 3. Polarization distributions in the equatorial cross-section of the nanoparticle with $R = 10$ nm, $\lambda = 0.03$ nm, $g_{44} = 2 \times 10^{-11}$ m^3/F, and room temperature 293 K. Cross-sections (a)-(f) correspond to different morphologies of the domain structure, namely, single-domain state (a), two-domain (b), three-domain (c), axially symmetric domains (d), multiple stripe domains (e), and labyrinthine domains (f). Top row shows initial seedings of the distributions shown in the lower row. The scale bar is for polarization P_3 in C/m^2. Values of the free energy G are listed below in 10^{-20} J. CIPS parameters are listed in Table I.

$0.02 < \lambda < 0.035$ nm. Coexistence of PDFE and PE phases when the nanoparticle consists of a PE surface layer and ferroelectric domain stripes in the core appears at $0.035 < \lambda < 0.045$ nm, and is followed by the size-induced phase transition into a stable PE phase at $\lambda > 0.045$ nm. Unexpectedly, we revealed a region of stable "labyrinthine" domains (LDs) of irregular shape (yellow circles) inside the region of regular domain structures with quadruple two (purple circles) or multiple (magenta circles) domain stripes. The LD region is within a dashed parallelogram in Fig. 2(a). We should underline that LD stability (or more rigorously speaking "long-living" metastabilty) does not mean their absolute stability, because we cannot make a sweep over all possible domain configurations to choose the one or several equivalent ones the energy of which reaches an absolute minimum.

With the temperature decrease from 293 K (that is very close to the CIPS Curie temperature 302 K) to 200 K the region of a SDFE significantly increases towards smaller radii R (up to the very small $R = 1$ nm for which LGD applicability becomes questionable) and higher λ (from, e.g., $\lambda = 0.003$ nm at 293 K to 0.02 nm at 200 K) [compare the size of SDFE regions in Figs. 2(a) and 2(b)]. The wide region of the PE phase (present at 293 K) almost disappears with the temperature decreasing to 200 K leading to the conclusion that the PDFE state can be stable in ultra-small CIPS nanoparticles (with radius less than 2 nm) covered by a screening charge [compare the size of PE regions in Figs. 2(a) and 2(b)]. The shift and increase of LD region(s) are evident with the temperature decrease from 300 to 200 K [compare the size and positions of LD regions in Figs. 2(a) and 2(b)]. The increase of SDFE, PDFE, and LD regions with temperature T decrease stems from the well-established fact that the FE phase becomes deeper and wider with the temperature increase, since the coefficient $\alpha = \alpha_T(T - T_C)$ acquires higher negative values with T decrease below Curie temperature T_C.

The effect of geometric catastrophe can be imagined from the images of LDs in the nanoparticles of radius 4, 3, and 2 nm for which the number of branches and sharp bendings of domain walls gradually decreases with the particle radius decrease from 4 to 2 nm [see right column in Fig. 2(b)]. Eventually the LD disappears for $R = 1$ nm. Hence the effect of geometric catastrophe suppresses the LD in small particles.

Note the validity of our prediction regarding LD appearance and PDFE state conservation for nanoparticles of sizes more than $2R = 4$ nm, because they correspond to ten lattice constants or more. It is general opinion that the LGD approach can be valid only qualitatively for the sizes less than 10 lattice constants [16–20,22,30–33], and must be approved by *ab initio* calculations.

B. Labyrinthine domains stability and evolution

Polarization distributions in the equatorial cross-section of the nanoparticle with radius $R = 10$ nm, screening length $\lambda = 0.03$ nm, and room temperature are shown in Fig. 3. The top row shows initial seedings of the distributions shown in the lower row. The energy values computed for the single-domain [Fig. 3(a)], two-domain [Fig. 3(b)], three-domain [Fig. 3(c)], axially symmetric domain [Fig. 3(d)], eight-domain stripe [Fig. 3(e)], and labyrinthine domain structure [Fig. 3(f)] are $G = -5.98, -6.94, -7.08, -8.50, -8.55$, and -9.04 (in 10^{-20} J) at a fixed value of $g_{44} = 2 \times 10^{-11}$ m^3/F. Thus the "labyrinthine" structure has the minimal energy corresponding to the optimal balance between the gradient-correlation energy (1b) tending to minimize the area of the domain walls (and hence to decrease the number of them) and electrostatic energy (1c) decreasing with domain width decrease. Note that the walls of the LD are uncharged in the central part of the particle and become charged and broadened near its poles (see yellow-blue regions near the poles in Fig. 1(a) and Fig. S2 in Supplemental Material [60]), since their broadening causes the depolarization field decrease [64].

Since the problem (2) and (3) together with boundary conditions is axially symmetric (about the x_3 axis), one should try to find a solution with the same axial symmetry. Actually, before we "stumble" into LD and/or curved domain stripes, we specify the initial distribution of the domain structure in the form of axially symmetric distributions, e.g., in the form of

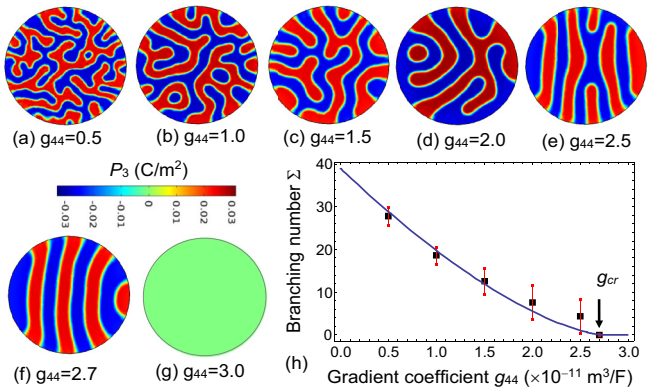

FIG. 4. Evolution of labyrinthine domain structure in a CIPS nanoparticle with increase of the gradient coefficient g_{44} (in 10^{-11} m^3/F) (a)–(g) for the screening length $\lambda = 0.03$ nm, radius $R = 10$ nm, and room temperature 293 K. The scale bar is the polarization value in C/m^2. (h) Dependence of the LD branching number Σ on g_{44}. Error bars correspond to different samples of LD emerging from different initial seeding. Black circles are averaged value $\langle\Sigma\rangle$ approximated by the function $\langle\Sigma\rangle = 39(1 - g_{44}/g_{cr})^{3/2}$ with $g_{cr} = 2.75 \times 10^{-11}$ m^3/F (blue curve). CIPS parameters are listed in Table I.

coaxial cylinders shown in the top row of Fig. 3(d). It appears that all radial structures are less stable than the stripes or irregular (labyrinth-like) structures [e.g., compare the energies of the final states in Figs. 3(d)–3(f)]. Radial distributions can relax to more stable distributions, and the relaxation rate depends on temperature, particle size, and surface screening length. To understand why the radial domain structure in the form of coaxial cylinders has higher energy than the stripes or LD, one can use simple geometric considerations showing that when all other conditions are equal (e.g., at the same distance between the domain walls) the radial domain structure has higher surface energy than the stripes or labyrinthine structures.

An example of labyrinthine domains evolution with increase of the gradient coefficient g_{44} is illustrated in Figs. 4(a)–4(e). Stable (in comparison with all other simulated domain structures) labyrinths exist at g_{44} less than the critical value $g_{cr} \approx 2.5 \times 10^{-11}$ m^3/F [Figs. 4(a)–4(e)], then they transform into quasiregular domain stripes [Fig. 4(f)], which in turn disappear with g_{44} increase more than 2.75×10^{-11} m^3/F [Fig. 4(g)]. Similarly, we made sampling over 5–20 different labyrinthine domain patterns for each g_{44}, R, and λ value, which emerged with computation time from different initial random distributions of polarization inside the particle (see Fig. S1 in Supplemental Material [60]). From Fig. S1 we concluded that the branching number Σ, defined as the total number of branched domain walls, dangling branches, separated stripes, and loops, decreases sharply with g_{44} increase. Σ varies slightly for different samples far from the critical value g_{cr} (top lines in Fig. S1), but the variation becomes bigger near the g_{cr} (bottom lines in Fig. S1).

Examples of Σ calculation are shown in Fig. 5. A color image of the complex labyrinthine pattern with dangling branches, branch seedings, separated island, and separated curved stripe is shown in Fig. 5(a). Figure 5(b) shows the black domains with white walls corresponding to the structure (a). Graphs (c) and (d) with numbered features have been drawn allowing for the connectivity between different domains and particle surface in plot 5(b). A proposed algorithm of Σ calculation counts all branching points, dangling branches, and separated stripes ends, which do not cross the particle from one surface to another one. Meanwhile the straight or slightly curved stripes (even very small) that cross the particle from one surface to another one do not contribute to Σ. However, the algorithm is not ideal, because the criteria distinguishing "slightly curved" and "strongly curved" stripes are somehow voluntary. Actually, for some complex cases, like the one shown in Fig. 5(a), visual recalculation of Σ leads to different results for peculiarities number corresponding to "red" ($\Sigma_r = 7$) and "blue" ($\Sigma_b = 9$) domains [compare Figs. 5(b) and 5(c)]. To improve the situation we operate with the values averaged for red and blue domains, e.g., $\Sigma = 8$ corresponds to Fig. 5(a).

Figure 5(e) has no relation to plot (a), but it is characteristic for the simpler domain patterns close to the transition to LD, where the accuracy in Σ calculation is the most important to establish the critical value g_{cr} correctly [compare Figs. 5(e) and 4(e)]. Figure 5(e) illustrates how the branching point (number 5), dangling branches (numbers 1 and 2), and separated stripe ends (numbers 3 and 4), which do not cross the particle from one surface to another one, contribute to Σ number. The other four slightly curved stripes, both ends of which are marked with asterisks "*" at particle surface, do not contribute to Σ number.

The sampling-averaged value $\langle\Sigma\rangle$ is not an integer for fixed g_{44}. From Fig. 4(h), the dependence of $\langle\Sigma\rangle$ on the gradient term g_{44} is described by the function $\langle\Sigma\rangle = 39(1 - g_{44}/g_{cr})^{3/2}$, and so it continuously appears at $g_{44} = g_{cr}$. Hence we can

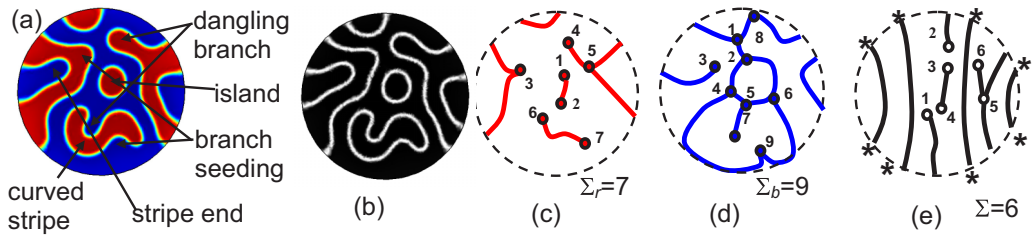

FIG. 5. Examples of Σ calculation using graph method. (a) A color image of the complex labyrinthine pattern with dangling branch, branch seeding, separated island, and separated curved stripe. (b) Black domains with white walls corresponding to the structure (a). Graphs (c) and (d) with numbered features have been drawn allowing for the connectivity between different domains and particle surface in plot (b). Graph (e) has no relation to plot (a), but it is characteristic for the patterns near the transition to LD state [compare Fig. 5(e) with Fig. 4(e)].

associate $\langle\Sigma\rangle$ appearance with a rapid change of the domain-wall connectivity.

We leave for further studies the question of how the threshold of labyrinthine domain appearance and the ranges of their stability at the phase diagram can be derived analytically.

The theoretical prediction of labyrinthine domains requires urgent verification by PFM, that is an ideal tool for three-dimensional visualization of the domain structure with nanoscale resolution (see, e.g., [8,63,65–67] and references therein). We are convinced by a numerical calculation that qualitatively similar LDs can be realized in other incompletely screened uniaxial ferroelectric nanoparticles, such as $Sn_2P_2(S, Se)_6$ and $LiNbO_3$, with the sizes near the first-order PE-FE transition. Notably the phase diagrams in Fig. 2 can change drastically for $\beta \geqslant 0$ corresponding to the second-order PE-FE transition. A much more complex situation (corresponding to the balance of labyrinthine domains in the bulk and vortices at the surface) is expected in multiaxial ferroelectric nanoparticles with polarization rotation allowed, such as $BaTiO_3$ and $BiFeO_3$, however we leave a discussion of these results for further studies.

IV. CONCLUSION

In the framework of the LGD approach combined with the equations of electrostatics, we studied the finite-size effects of the phase diagrams and domain structure in spherical ferroelectric nanoparticles covered by a layer of a screening charge with finite screening length. The phase diagrams, calculated in coordinates particle radius and screening length, has a wide region of versatile polydomain states separating single-domain ferroelectric and nonpolar paraelectric phases. Quite unexpectedly we revealed that a regular stripe domain structure sharply transforms into a labyrinth pattern with a gradient term decrease below the critical value and named the event as a gradient-driven transition. Obtained results calculated for $CuInP_2S_6$ can be readily generalized for other incompletely screened nanoparticles of uniaxial ferroelectrics with the first-order transition to the paraelectric phase.

ACKNOWLEDGMENTS

S.V.K. and P.M. were supported by the U.S. Department of Energy (DOE), Office of Basic Energy Sciences, Materials Sciences and Engineering Division under the Grant No. DEAC0500OR22725. A portion of this research was conducted at the Center for Nanophase Materials Sciences, which is a DOE Office of Science User Facility. A.N.M. was partially supported by the National Academy of Sciences of Ukraine (Projects No. 0118U003375 and No. 0117U002612) and by the Program of Fundamental Research of the Department of Physics and Astronomy of the National Academy of Sciences of Ukraine (Project No. 0117U000240).

E.A.E. wrote the codes, performed numerical calculations, and prepared figures. Y.M.F. tested the codes and assisted E.A.E. with simulations. A.N.M. generated the research idea, stated the problem, interpreted results, and wrote the paper. S.V.K., Y.M.V., and P.M. worked on the results discussion and paper improvement.

[1] N. D. Mermin, The topological theory of defects in ordered media, Rev. Mod. Phys. **51**, 591 (1979).

[2] *Topological Structures in Ferroic Materials*, edited by J. Seidel, Springer Series in Materials Science Vol. 228 (Springer, New York, 2016), p. 181.

[3] A. Gruverman, D. Wu, H.-J. Fan, I. Vrejoiu, M. Alexe, R. J. Harrison, and J. F. Scott, Vortex ferroelectric domains, J. Phys.: Condens. Matter **20**, 342201 (2008).

[4] N. Balke, B. Winchester, W. Ren, Y. Hao Chu, A. N. Morozovska, E. A. Eliseev, M. Huijben, R. K. Vasudevan, P. Maksymovych, J. Britson, S. Jesse, I. Kornev, R. Ramesh, L. Bellaiche, L.-Q. Chen, and S. V. Kalinin, Enhanced electric conductivity at ferroelectric vortex cores in $BiFeO_3$, Nat. Phys. **8**, 81 (2012).

[5] B. Winchester, N. Balke, X. X. Cheng, A. N. Morozovska, S. Kalinin, and L. Q. Chen, Electroelastic fields in artificially created vortex cores in epitaxial $BiFeO_3$ thin films, Appl. Phys. Lett. **107**, 052903 (2015).

[6] I. I. Naumov, L. Bellaiche, and H. Fu, Unusual phase transitions in ferroelectric nanodisks and nanorods, Nature (London) **432**, 737 (2004).

[7] A. K.Yadav, C. T. Nelson, S. L. Hsu, Z. Hong, J. D. Clarkson, C. M. Schlepütz, A. R. Damodaran, P. Shafer, E. Arenholz, L. R. Dedon, D. Chen, A. Vishwanath, A. M. Minor, L. Q. Chen, J. F. Scott, L. W. Martin, and R. Ramesh, Observation of polar vortices in oxide superlattices, Nature (London) **530**, 198 (2016).

[8] A. Kholkin, A. Morozovska, D. Kiselev, I. Bdikin, B. Rodriguez, P. Wu, A. Bokov, Z.-G. Ye, B. Dkhil, L.-Q. Chen, M. Kosec, and S. V. Kalinin. Surface domain structures and mesoscopic phase transition in relaxor ferroelectrics, Adv. Func. Mat. **21**, 1977 (2011).

[9] G. Catalan, H. Béa, S. Fusil, M. Bibes, P. Paruch, A. Barthélémy, and J. F. Scott, Fractal Dimension and Size Scaling of Domains in Thin Films of Multiferroic $BiFeO_3$, Phys. Rev. Lett. **100**, 027602 (2008).

[10] S. V. Kalinin, B. J. Rodriguez, J. D. Budai, S. Jesse, A. N. Morozovska, A. A. Bokov, and Z. G. Ye, Direct evidence of mesoscopic dynamic heterogeneities at the surfaces of ergodic ferroelectric relaxors, Phys. Rev. B **81**, 064107 (2010).

[11] V. V. Shvartsman and A. L. Kholkin, Domain structure of $(Pb(Mg_{1/3}Nb_{2/3})O_3)_{0.8}(PbTiO_3)_{0.2}$ studied by piezoresponse force microscopy, Phys. Rev. B **69**, 014102 (2004).

[12] K. S. Wong, J. Y. Dai, X. Y. Zhao, and H. S. Luo, Time- and temperature-dependent domain evolutions in poled (111)-cut $(Pb(Mg_{1/3}Nb_{2/3})O_3)_{0.7}(PbTiO_3)_{0.3}$ single crystal, Appl. Phys. Lett. **90**, 162907 (2007).

[13] A. N. Morozovska, E. A. Eliseev, J. Wang, G. S. Svechnikov, Yu. M. Vysochanskii, V. Gopalan, and L.-Q. Chen, Phase diagram and domain splitting in thin ferroelectric films with incommensurate phase, Phys. Rev. B **81**, 195437 (2010).

[14] A. Artemev, B. Geddes, J. Slutsker, and A. Roytburd, Thermodynamic analysis and phase field modeling of domain structures

in bilayer ferroelectric thin films, J. Appl. Phys. **103**, 074104 (2008).

[15] A. Hubert and R. Schafer, *Magnetic Domains: The Analysis of Magnetic Microstructures* (Springer, New York, 1998).

[16] D. Yadlovker and S. Berger, Uniform orientation and size of ferroelectric domains, Phys. Rev. B **71**, 184112 (2005).

[17] D. Yadlovker and S. Berger, Reversible electric field induced nonferroelectric to ferroelectric phase transition in single crystal nanorods of potassium nitrate, Appl. Phys. Lett. **91**, 173104 (2007).

[18] D. Yadlovker and S. Berger, Nucleation and growth of single crystals with uniform crystallographic orientation inside alumina nanopores, J. Appl. Phys. **101**, 034304 (2007).

[19] M. H. Frey and D. A. Payne, Grain-size effect on structure and phase transformations for barium titanate, Phys. Rev. B **54**, 3158 (1996).

[20] Z. Zhao, V. Buscaglia, M. Viviani, M. T. Buscaglia, L. Mitoseriu, A. Testino, M. Nygren, M. Johnsson, and P. Nanni, Grain-size effects on the ferroelectric behavior of dense nanocrystalline $BaTiO_3$ ceramics, Phys. Rev. B **70**, 024107 (2004).

[21] A. V. Drobnich, A. A. Molnar, A. V. Gomonnai, Yu. M. Vysochanskii, and I. P. Prits, The effect of size factor on the phase transition in $Sn_2P_2S_6$ crystals: Experimental data and simulation in ANNNI model, Cond. Matt. Phys. **6**, 205 (2003).

[22] E. Erdem, H.-Ch. Semmelhack, R. Bottcher, H. Rumpf, J. Banys, A. Matthes, H.-J. Glasel, D. Hirsch, and E. Hartmann, Study of the tetragonal-to-cubic phase transition in $PbTiO_3$ nanopowders, J. Phys.: Condens. Matter **18**, 3861 (2006).

[23] I. S. Golovina, V. P. Bryksa, V. V. Strelchuk, I. N. Geifman, and A. A. Andriiko, Size effects in the temperatures of phase transitions in $KNbO_3$ nanopowder, J. Appl. Phys. **113**, 144103 (2013).

[24] I. S. Golovina, V. P. Bryksa, V. V. Strelchuk, and I. N. Geifman, Phase transitions in the nanopowders $KTa_{0.5}Nb_{0.5}O_3$ studied by Raman spectroscopy, Funct. Mater. **20**, 75 (2013).

[25] I. S. Golovina, B. D. Shanina, S. P. Kolesnik, I. N. Geifman, and A. A. Andriiko, Magnetic properties of nanocrystalline $KNbO_3$, J. Appl. Phys. **114**, 174106 (2013).

[26] P. Perriat, J. C. Niepce, and G. Caboche, Thermodynamic considerations of the grain size dependency of material properties: a new approach to explain the variation of the dielectric permittivity of $BaTiO_3$ with grain size, J. Therm. Anal. Calorim. **41**, 635 (1994).

[27] H. Huang, C. Q. Sun, and P. Hing, Surface bond contraction and its effect on the nanometric sized lead zirconate titanate, J. Phys.: Condens. Matter **12**, L127 (2000).

[28] H. Huang, C. Q. Sun, Z. Tianshu, and P. Hing, Grain-size effect on ferroelectric $Pb(Zr_{1-x}Ti_x)O_3$ solid solutions induced by surface bond contraction, Phys. Rev. B **63**, 184112 (2001).

[29] Wenhui Ma, Surface tension and Curie temperature in ferroelectric nanowires and nanodots, Appl. Phys. A **96**, 915 (2009).

[30] E. A. Eliseev, A.N. Morozovska, M. D. Glinchuk, and R. Blinc, Spontaneous flexoelectric/flexomagnetic effect in nanoferroics, Phys. Rev. B **79**, 165433 (2009).

[31] A. N. Morozovska, E. A. Eliseev, and M. D. Glinchuk, Ferroelectricity enhancement in confined nanorods: Direct variational method, Phys. Rev. B **73**, 214106 (2006).

[32] A. N. Morozovska, M. D. Glinchuk, and E. A. Eliseev, Phase transitions induced by confinement of ferroic nanoparticles, Phys. Rev. B **76**, 014102 (2007).

[33] A. N. Morozovska, I. S. Golovina, S. V. Lemishko, A. A. Andriiko, S. A. Khainakov, and E. A. Eliseev, Effect of Vegard strains on the extrinsic size effects in ferroelectric nanoparticles, Phys. Rev. B **90**, 214103 (2014).

[34] J. Wang, A. K. Tagantsev, and N. Setter, Size effect in ferroelectrics: Competition between geometrical and crystalline symmetries, Phys. Rev. B **83**, 014104 (2011).

[35] E. A. Eliseev, A. V. Semchenko, Y. M. Fomichov, M. D. Glinchuk, V. V. Sidsky, V. V. Kolos, Yu. M. Pleskachevsky, M. V. Silibin, N. V. Morozovsky, and A. N. Morozovska, Surface and finite size effects impact on the phase diagrams, polar, and dielectric properties of (Sr, Bi)Ta_2O_9 ferroelectric nanoparticles, J. Appl. Phys. **119**, 204104 (2016).

[36] V. V. Khist, E. A. Eliseev, M. D. Glinchuk, D. V. Karpinsky, M. V. Silibin, and A. N. Morozovska, Size effects of ferroelectric and magnetoelectric properties of semi-ellipsoidal bismuth ferrite nanoparticles, J. Alloys Compd. **714**, 303 (2017).

[37] C.-G. Duan, S. S. Jaswal, and E. Y. Tsymbal, Predicted Magnetoelectric Effect in Fe/$BaTiO_3$ Multilayers: Ferroelectric Control of Magnetism, Phys. Rev. Lett. **97**, 047201 (2006).

[38] G. Geneste, E. Bousquest, J. Junquera, and P. Ghosez, Finite-size effects in $BaTiO_3$ nanowires, Appl. Phys. Lett. **88**, 112906 (2006).

[39] M. Q. Cai, Y. Zheng, B. Wang, and G. W. Yang, Nanosize confinement induced enhancement of spontaneous polarization in a ferroelectric nanowire, Appl. Phys. Lett. **95**, 232901 (2009).

[40] J. W. Hong, G. Catalan, D. N. Fang, E. Artacho, and J. F. Scott, Topology of the polarization field in ferroelectric nanowires from first principles, Phys. Rev. B **81**, 172101 (2010).

[41] E. Bousquet, N. Spaldin, and Ph. Ghosez, Strain-Induced Ferroelectricity in Simple Rocksalt Binary Oxides, Phys. Rev. Lett. **104**, 037601 (2010).

[42] C. L. Wang and S. R. P. Smith, Landau theory of the size-driven phase transition in ferroelectrics, J. Phys.: Condens. Matter **7**, 7163 (1995).

[43] A. N. Morozovska, E. A. Eliseev, R. Blinc, and M. D. Glinchuk, Analytical prediction of size-induced ferroelectricity in BaO nanowires under stress, Phys. Rev. B **81**, 092101 (2010).

[44] A. Sundaresan, R. Bhargavi, N. Rangarajan, U. Siddesh, and C. N. R. Rao, Ferromagnetism as a universal feature of nanoparticles of the otherwise nonmagnetic oxides, Phys. Rev. B **74**, 161306(R) (2006).

[45] D. D. Fong, G. B. Stephenson, S. K. Streiffer, J. A. Eastman, O. Auciello, P. H. Fuoss, and C. Thompson, Ferroelectricity in ultrathin perovskite films, Science **304**, 1650 (2004).

[46] J. Bardeen, Surface states and rectification at a metal semiconductor contact, Phys. Rev. **71**, 717 (1947).

[47] V. M. Fridkin, *Ferroelectric Semiconductors* (Consultant Bureau, New York and London, 1980).

[48] M. A. Itskovsky, Some peculiarities of phase transition in thin layer ferroelectric, Fiz. Tv. Tela **16**, 2065 (1974).

[49] P. W. M. Blom, R. M. Wolf, J. F. M. Cillessen, and M. P. C. M. Krijn, Ferroelectric Schottky Diode, Phys. Rev. Lett. **73**, 2107 (1994).

[50] A. N. Morozovska, E. A. Eliseev, S. V. Svechnikov, A. D. Krutov, V. Y. Shur, A. Y. Borisevich, P. Maksymovych, and S. V. Kalinin, Finite size and intrinsic field effect on the polar-active properties of ferroelectric semiconductor heterostructures, Phys. Rev. B **81**, 205308 (2010).

[51] Y. A. Genenko, O. Hirsch, and P. Erhart, Surface potential at a ferroelectric grain due to asymmetric screening of depolarization fields, J. Appl. Phys. **115**, 104102 (2014).

[52] G. B. Stephenson and M. J. Highland, Equilibrium and stability of polarization in ultrathin ferroelectric films with ionic surface compensation, Phys. Rev. B **84**, 064107 (2011).

[53] M. J. Highland, T. T. Fister, D. D. Fong, P. H. Fuoss, C. Thompson, J. A. Eastman, S. K. Streiffer, and G. B. Stephenson, Equilibrium Polarization of Ultrathin $PbTiO_3$ with Surface Compensation Controlled by Oxygen Partial Pressure, Phys. Rev. Lett. **107**, 187602 (2011).

[54] S. V. Kalinin, Y. Kim, D. Fong, and A. Morozovska, Surface screening mechanisms in ferroelectric thin films and its effect on polarization dynamics and domain structures, Rep. Prog. Phys. **81**, 036502 (2018).

[55] A. K. Tagantsev and G. Gerra, Interface-induced phenomena in polarization response of ferroelectric thin films, J. Appl. Phys. **100**, 051607 (2006).

[56] Y. Gu, M. Li, A. N. Morozovska, Y. Wang, E. A. Eliseev, V. Gopalan, and L.-Q. Chen, Non-Ising character of a ferroelectric wall arises from a flexoelectric effect, Phys. Rev. B **89**, 174111 (2014).

[57] A. N. Morozovska, E. A. Eliseev, Y. A. Genenko, I. S. Vorotiahin, M. V. Silibin, Y. Cao, Y. Kim, M. D. Glinchuk, and S. V. Kalinin, Flexocoupling impact on the size effects of piezo- response and conductance in mixed-type ferroelectrics-semiconductors under applied pressure, Phys. Rev. B **94**, 174101 (2016).

[58] I. S. Vorotiahin, E. A. Eliseev, Q. Li, S. V. Kalinin, Yu. A. Genenko, and A. N. Morozovska, Tuning the polar states of ferroelectric films via surface charges and flexoelectricity, Acta Mater. **137**, 85 (2017).

[59] E. A. Eliseev, I. S. Vorotiahin, Y. M. Fomichov, M. D. Glinchuk, S. V. Kalinin, Yu. A. Genenko, and A. N. Morozovska, Defect driven flexo-chemical coupling in thin ferroelectric films, Phys. Rev. B **97**, 024102 (2018).

[60] See Supplemental Material at http://link.aps.org/supplemental/10.1103/PhysRevB.98.054101 for results.

[61] A. Belianinov, Q. He, A. Dziaugys, P. Maksymovych, E. Eliseev, A. Borisevich, A. Morozovska, J. Banys, Y. Vysochanskii, and S. V. Kalinin, $CuInP_2S_6$ room temperature layered ferroelectric, Nano Lett. **15**, 3808 (2015).

[62] Note that the coefficient g_{44} rules the polarization behavior, since this coefficient determines the energy of uncharged domain walls. Since g_{11} is not small and positive for CIPS (it is five times higher than g_{44}) its influence appears much less important even at the particle surface, and the next positive gradient terms add almost nothing to the physical picture we calculated. Also, we supposed isotropic properties in the (001) plane, $g_{44} = g_{55}$.

[63] S. V. Kalinin, A. N. Morozovska, L.-Q. Chen, and B. J. Rodriguez, Local polarization dynamics in ferroelectric materials, Rep. Prog. Phys. **73**, 056502 (2010).

[64] E. A. Eliseev, A. N. Morozovska, S. V. Kalinin, Y. Li, J. Shen, M. D. Glinchuk, L.-Q. Chen, and V. Gopalan, Surface effect on domain wall width in ferroelectrics, J. Appl. Phys. **106**, 084102 (2009).

[65] A. Gruverman, O. Auciello, and H. Tokumoto, Imaging and control of domain structures in ferroelectric thin films via scanning force microscopy, Annu. Rev. Mater. Sci. **28**, 101 (1998).

[66] A. Gruverman and A. Kholkin, Nanoscale ferroelectrics: Processing, characterization and future trends, Rep. Prog. Phys. **69**, 2443 (2006).

[67] V. V. Shvartsman and A. L. Kholkin, Evolution of nanodomains in $0.9PbMg_{1/3}Nb_{2/3}O_3$-$0.1PbTiO_3$ single crystals, J. Appl. Phys. **101**, 064108 (2007).